Received: 17 May 2021 | Revised: 10 August 2021 | Accepted: 14 September 2021

DOI: 10.1002/aic.17452

TRANSPORT PHENOMENA AND FLUID MECHANICS

AIChE JOURNAL

Scalable 3D-printed lattices for pressure control in fluid applications

Ian R. Woodward | Lucas Attia | Premal Patel | Catherine A. Fromen

Department of Chemical and Biomolecular Engineering, University of Delaware, Delaware, USA

Correspondence
Catherine A. Fromen, Department of Chemical and Biomolecular Engineering, University of Delaware, Newark, DE, USA.
Email: cfromen@udel.edu

Funding information
National Institute of General Medical Sciences, Grant/Award Numbers: P20GM104316, U54-GM104941

Abstract

Additive manufacturing affords precise control over geometries with high degrees of complexity and predefined structure. Lattices are one class of additive-only structures which have great potential in directing transport phenomena because they are highly ordered, scalable, and modular. However, a comprehensive description of how these structures scale and interact in heterogeneous systems is still undetermined. To advance this aim, we designed cubic and Kelvin lattices at two sub-5-mm length scales and compared published correlations to the experimental pressure gradient in pipes ranging from 12 to 52 mm diameter. We further investigated all combinations of the four lattices to evaluate segmented combinatorial behavior. The results suggest that a single correlation can describe pressure behavior for different lattice geometries and scales. Furthermore, combining lattice systems in series has a complex effect that is sensitive to part geometry. Together, these developments support the promise for tailored, modular lattice systems at laboratory scales and beyond.

KEYWORDS
3D printing, lattices, open cellular structures, pressure drop, scaling

1 | INTRODUCTION

In recent years, 3D printing has seen rapid proliferation with respect to printing techniques, material selection, and overall access, enabling new insights and innovations across a range of disciplines.[1–3] Increased interest in these technologies has driven the viability of additive manufacturing and enabled novel approaches to chemical engineering challenges, including heat exchanger design, reaction engineering, drug delivery, and more.[4–7] With its nearly infinite design space, 3D printing technology is evolving alongside new software tools to design, simulate, and realize concepts that could previously be only theorized.[8–10] There is growing precedent for using additively manufactured parts for controlling fluid transport, including multioutlet and mulitinlet devices for a range of applications.[11–14] Such works demonstrate the potential for 3D printing and additive manufacturing to drive novel transport process development and new applications, enabled by the complex structures that only additive processes can produce.

Lattices, sometimes referred to as metamaterials, are one such class of additive-only designs. Similar to foams, lattices are high-porosity, strut-based structures.[15] Unlike their stochastic counterparts, lattices can be designed with defined dimensions in an ordered arrangement. However, while additively manufactured lattices and periodic structures have been explored in detail for their mechanical and thermal properties, their use in fluid applications remains a high-potential area.[16–22] Much of the recent investigation into lattices for fluid applications have emerged from studies of open-cell foams. Because their structures can be defined a priori and remain static, additively manufactured periodic structures, encompassing beam lattices, surface lattices, and arranged polyhedra, have emerged as a viable option for creating rationally designed, ordered packings with tunable porosity and surface area (Figure 1). These are valuable attributes for chromatography and separations processes, where the ability to generate an ordered bed facilitates numerical simulation and comparison between packing geometries.[23,24] Furthermore, given their foam likeness, beam lattices can also be used as platforms for catalytic process intensification, where they have been shown to have desirable catalytic performance even with lower surface area than honeycombs.[25–27] These structures can also be functionalized with

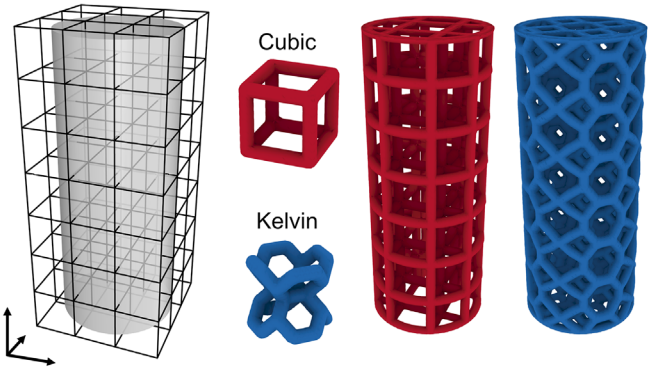

FIGURE 1 Parts made in CAD are discretized into regular volumetric regions and populated with repeating geometries to create lattice structures. Lattices are a unique construct of additive manufacturing, useful for a variety of chemical engineering applications in catalysis, fluid transport, and separations. Cubic (left, red) and Kelvin (right, blue) lattices are investigated in this work. CAD, computer-aided design [Color figure can be viewed at wileyonlinelibrary.com]

high-surface-area materials or other coatings to achieve additional properties.[28] The most commonly studied structures in this field are the cubic unit cell lattice, due it its simplicity in design and production, and the Kelvin cell lattice, which represents the idealization of commonly used stochastic foam structures.[29,30] The advantages of using these structures as porous media are that they are easily lent to systematic study and modification and, because they are able to achieve high surface areas with low porosity and tortuosity, they result in lower pressure drop and energy loss than stochastic open-cell foams.[31] Notably, recent work has highlighted the potential uses for lattices in cellular fluidics applications, where lattice design parameters can be selected to tune capillary action and evaporation, among other phenomena.[32]

However, the vast design space can also be a barrier to adoption. The predefined order of these structures is useful for describing the internal geometry, but the trimming patterns created in functional parts can lead to varying influences of the walls in fluid systems. Describing the flow profiles evolving from the existing transport phenomena and wall contributions at various internal and overall scales is necessary for developing design strategies that can produce highly specified parts that address unique process needs. Despite this, the majority of investigations have focused on similar system sizes, length scales, and homogeneous packing types. Another distinct advantage of additive manufacturing is the ability to combine multiple components into a single part or create regions for interchangeable components. In the context of chemical engineering, this technology could streamline multiple processing operations into a single component, reduce changeover time, and facilitate scalable distributed production. Despite these advantages, it is not well understood how combination structures influence local behavior or overall fluid phenomena. Thus, while many predictive correlations exist for different types of packing geometries, a unifying model has yet to be presented to account for the varieties of highly ordered packing geometry and range of internal and external scales.

In this work, we investigate fluid transport properties to consider scaling and combinatorial effects in two common geometries that juxtapose additive lattices and traditional foams. For cubic and Kelvin lattice geometries, we examine geometrical similarity at various internal and overall scales, how their respective airflow and pressure behaviors align with model predictions, and how combinations of these lattice structures influence fluid phenomena in a hybrid lattice system. These results build toward harnessing the full potential of additive manufacturing for realizing on-demand fluid control systems for a host of applications at laboratory scales and beyond.

2 | MATERIALS AND METHODS

2.1 | Lattice models

For printed lattice structures, cubic and Kelvin unit cell geometries were created using the computer-aided design (CAD) software Rhinoceros 3D and Grasshopper (Robert McNeel & Associates) using internal scripts and the Crystallon (*f=f*) and Dendro (ECR Labs) plugins. Each structure was based on a repeat unit with equal edge lengths. Lattice trimming was performed to create a conformal cylindrical monolith while maintaining lattice connectivity at the trimmed boundaries, in order to print each part without supports. These structures were generated for two unit cell length scales (2.38 and 4.49 mm, designated S and L) and three pipe scales (overall diameter = 12.2, 34.1, and 52.05 mm). For single-lattice monoliths, the part was designed with 100 mm length. To reduce mesh size, the 52.05-mm Kelvin-S lattice was designed with 50 mm length. Combination monoliths were designed at 50 and 100 mm overall length to fit the 12.2-mm system. Naming conventions for the combination lattices follow the format, lattice geometry—cell size, using abbreviations for each. For example, the combination of a Kelvin lattice with small cell length and a cubic lattice with large cell length is designated as KSCL or Kelvin-S|Cubic-L. For each lattice configuration, the input characteristics, volume, and surface area were quantified in the CAD software and used to determine the geometric quantities of interest. These quantities were also determined for lattice structures at a single-cell scale using an internal script for automation. Characteristics of interest included cell length (l_c), strut radius (r), dimensionless strut radius ($r^* = r/l_c$), porosity (ε), specific surface area based on the overall bounding volume (a_v), and hydraulic diameter (d_h). All parts in this study were designed with $r^* = 0.11$. Other part dimensions are further detailed in Table 1.

2.2 | 3D printing

3D printing was performed by digital light synthesis (DLS™) on a Carbon M1 3D printer (Carbon, Inc.) with XY resolution 75 × 75 μm. All parts were printed using the proprietary material UMA 90 Black, a one-part, photocurable resin. Parts were arranged and sliced using

TABLE 1 Calculated geometric properties based on CAD dimensions

Lattice	Pipe diameter (mm)	ε CAD (CT)	$a_{v,total}$ (m^{-1}) CAD (CT)	$d_{p,eq}$ (mm)	d_h (mm)
Cubic-S	12.2	0.887 (0.911)	1200 (1055)	0.567	2.95
	34.1	0.897	890	0.692	4.03
	52.05	0.904	804	0.718	4.50
Cubic-L	12.2	0.843 (0.877)	936 (860)	1.004	3.61
	34.1	0.873	590	1.288	5.92
	52.05	0.896	493	1.268	7.26
Kelvin-S	12.2	0.756 (0.762)	1938 (1874)	0.754	1.56
	34.1	0.753	1739	0.851	1.73
	52.05	0.766	1624	0.864	1.89
Kelvin-L	12.2	0.711 (0.717)	1298 (1282)	1.338	2.19
	34.1	0.752	983	1.516	3.06
	52.05	0.758	915	1.587	3.31

Note: Lattices designated (S) generated with a unit cell length of 2.38 mm and strut radius of 0.262 mm; lattices designated (L) generated with a unit cell length of 4.49 mm and strut radius of 0.494 mm. Values measured from CT scans are indicated for the smallest diameter lattices in each configuration; CT-scaled values and derived values are omitted for clarity.
Abbreviations: CAD, computer-aided design; CT, computed tomography.

Carbon's cloud 3D printing software, with a vertical resolution of 100 μm. Parts were processed in line with manufacturer recommendations, which included washing in 2-propanol (IPA, Fisher Chemical) for approximately 5 min, drying with compressed air, and curing for 1 min per side. Parts were allowed to equilibrate from solvent exposure for at least 24 h before testing.

2.3 | X-ray computed tomography

X-ray computed tomography (CT) was performed on a Bruker SkyScan 1276 (Bruker Corporation) at a nominal scan resolution of 21 μm. The scan conditions used a 0.25-mm aluminum (Al) target with 200 μA at 55 kV, for 180° rotation about the sample at 0.3° per step. The exposure time for each image was approximately 340 ms. The smallest diameter lattices were scanned in a region approximately 20 mm in length at the center of the part for representative results. CT processing was performed using the NRecon software (Bruker Corporation). Reconstruction was performed using 3D Slicer v4.10.2.[33] The Fast Marching segmentation algorithm was used on the region of interest with increasing thresholding parameters until nonphysical image artifacts (noise) began to appear in the body and on the surface of the 3D reconstruction. After thresholding, the 3D model was generated using the default settings (0.5 smoothing and 0 decimation), and the surface area and volume of the part were quantified in 3D Slicer.

2.4 | Pressure measurement

Pressure gradient was measured for latticed parts in three pipe diameters (*D*; 12.2, 34.1, and 52.05 mm). Example lattice parts and a system

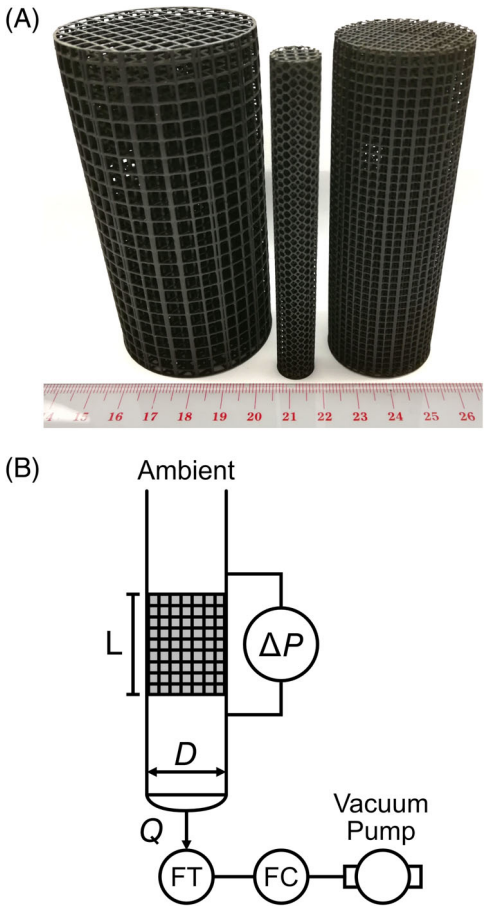

FIGURE 2 (A) Photograph of 3D-printed lattices at each pipe scale. Image enhanced for clarity. (B) Diagram of the experimental system used in measuring the pressure gradient across each lattice. Pressure taps were placed at 0.6*D* upstream and downstream of the 100-mm measurement zone. FC, flow controller; FT, flow transmitter [Color figure can be viewed at wileyonlinelibrary.com]

diagram are shown in Figure 2. All pipes were approximately 0.6 m in length. Each pipe was mounted vertically, with a removable fitting at the bottom for inserting and removing lattice samples. Pressure taps were placed on either side of a 100-mm sample region for each pipe, in line with previous experimental methods for cubic lattice and foam measurements.[29,34] The upstream and downstream distance from the sample region scaled with the pipe diameter at approximately 0.6*D*. For each experiment, the lattice sample was wrapped with tape on both ends to ensure a secure fit within the measurement zone. After aligning the sample, the pipe was connected inline with a mass flow meter (Model 4043, TSI, Inc.), flow controller (TPK 2000, Copley Scientific, Ltd), and vacuum pump (HCP5, Copley Scientific, Ltd). The flow meter was calibrated to report the volumetric flow rate in standard liters per minute at 0°C and atmospheric pressure. A Dwyer Magnehelic differential pressure and vacuum gauge (0–248.84 Pa, ±2%, Dwyer Instruments, Inc.) or a Dwyer Magnehelic differential pressure gauge (0–62.21 Pa, ±4%; 746.52 Pa, ±2%) was connected to the pressure taps using flexible tubing and used for measuring the pressure gradient across the measurement zone. The flow controller was set manually over the range of measurable pressures, and the pressure differential and flow rate were recorded for 11 pressure gradient set points in the 0–248.84 Pa range for all lattices. Additional data series were collected for the 12-mm lattices to expand the observed Reynolds number (*Re*) range. Respectively, additional data were collected in the 0–62.21 Pa range for cubic lattices and the both the 0–61.21 and 0–746.52 Pa ranges for Kelvin lattices. For cubic lattices in the larger pipe scales, a limited set of measurements was taken due to low pressure gradients at the maximum flow rate. For other lattice parts, two replicate measurements were taken at each set point. First, the flow controller was set to the maximum opening, and measurements were recorded at regular decreasing intervals until the valve was closed. The same measurements were repeated, starting with the valve fully closed and increasing the system flow rate.

2.5 | Analytical models and statistical analysis

Data were analyzed using R v3.6.3 (R Foundation for Statistical Computing). Experimental data were compared to the analytical correlations presented for cubic lattices by Klumpp et al.[29] or foams, presented by Inayat et al.[30] The periodic open cellular structure (POCS) model was derived for a range of cubic geometries and considers the pressure gradient as a function of exclusively inertial contributions.[29] Equation (1) describes the reduced model used for comparison in this study.

$$\frac{\Delta P}{L} = \left(\frac{\varepsilon_A}{1-\varepsilon_A}\right)\left(\frac{1-\varepsilon}{\varepsilon}\right)\frac{\rho \cdot a_v}{\varepsilon^3}u^2, \tag{1}$$

where ε_A is the area porosity or void fraction of the open area projected in the flow direction (with complete line of sight from one end of the structure to the other), ε is the void fraction for the total the system, ρ is the fluid density, a_v is the specific surface area on a total volume basis, and u is the superficial velocity. The authors of this model make additional provisions for structures with a rotated unit cell, which is beyond the scope of this work.[29]

The foam model, developed by the same research group, considers the pressure drop through an idealized foam based on the Kelvin geometry, consisting of both viscous and inertial contributions. Equation (2) describes the form of the foam model and its tortuosity definition (Equation 3).

$$\frac{\Delta P}{L} = 32\tau^2 \frac{\mu}{\varepsilon \cdot d_h^2}u + \frac{\tau^3}{2}\frac{\rho}{\varepsilon^2 \cdot d_h}u^2, \tag{2}$$

$$\tau \equiv 1 + \frac{d_w \cdot a_v}{4\varepsilon}, \tag{3}$$

where τ is the tortuosity, defined for an equivalent bundle of tubes, μ is the fluid viscosity, d_h is the hydraulic diameter, and d_w is the window diameter of the foam. All other terms are common between the two equations. For analysis of the flow regime, the packed bed Reynolds number (Re_p) and packed bed friction factor (f^*) are defined by the following:

$$Re_p = \frac{d_{p,eq} \cdot u \cdot \rho}{\mu(1-\varepsilon)}, \tag{4}$$

$$f^* = \frac{\Delta P}{L}\frac{d_{p,eq} \cdot \varepsilon^3}{(1-\varepsilon) \cdot \rho \cdot u^2}. \tag{5}$$

Experimental data were also considered using standard linear models and analysis of variance (ANOVA) techniques. Pressure gradient profiles ($\Delta P/L$, Pa/m) were modeled as a parabolic function of superficial velocity (u, m/s). Regression estimates were evaluated for significance by t tests. Orientation significance was evaluated by developing a linear regression including a term for orientation (treatments centered about 0 at ±1), including all terms for the interaction between orientation and the superficial velocity polynomial. Orientation significance was determined by performing ANOVA on the full model and nested model with no interaction terms, to evaluate whether inclusion of the additional parameters was concomitant with error reduction; the significance of the ANOVA was considered along with the significance of the coefficients to determine the effects of stack orientation, taking $p < 0.05$ as a guide for statistical significance. A similar approach was used to evaluate significant differences between pressure gradients across pipe scales. A list of all R packages used and full model details are included in Section 1 of Data S1, and statistical analyses are included in Section 8 of Data S1.

2.6 | Tortuosity estimation

In testing various inputs to the analytical models, we developed a procedure for estimating tortuosity based on the geometry of a single unit cell. Briefly, a grid array of lines was generated within the unit

cell, passing from the top face of the bounding volume to the bottom face. The lattice structure was situated in the same orientation as the experimental studies. The lines were classified according to their intersection with the geometry, and regions contained within the lattice were projected onto the closest beam surface. With all lines passing through open areas or along the geometry surface, a weighted average of line lengths was normalized by the unit cell edge length to determine the tortuosity estimate. This process is discussed in more detail in Section 4 of Data S1.

3 | RESULTS AND DISCUSSION

3.1 | Lattice characterization

Cellular structures for 3D printing are comprised of a vast design space but can be often specified with a smaller number of parameters. Unit cell geometry, unit cell size, and element thickness are commonly used for designing these structures in primitive and functional forms. Previous reports have defined a variation of the specific length ratio ($l_c/2r$) to describe the asymptotic behavior of properties like porosity and specific surface area.[29,35] These descriptions do well to illustrate the limits of such properties. However, they fail to relate these geometric characteristics to the design process and the bounded nature of the printable design space. First, lattice generation typically begins with spatial discretization, which takes cell size as an input. Second, the strut dimension in most beam-based lattices will not exceed the cell size without intersecting other struts and blocking flow through the structure. In this regard, the critical radius values for closure depend on the unit cell geometry. Finally, strut dimension will be closer to the limiting feature sizes of an additive process. Therefore, the strut dimension will be more sensitive to deviation than the cell size. As a result, the cell length (l_c) more naturally emerges as a reference length scale for comparing lattice configurations between strut dimensions and unit cell geometries. Here, we selected the dimensionless strut radius ($r^* = r/l_c$) to investigate theoretical geometric quantities for the cubic and Kelvin cells based on CAD geometry. Taken in conjunction with experimental process knowledge, the resultant trends in porosity, specific surface area, and hydraulic diameter can facilitate the selection between unit cell geometries and lattice configurations.

Theoretical porosity and specific surface area based on CAD calculations for a range of cell lengths across both unit cells are shown in Figure 3A,B. Between both geometries, porosity takes a constant value for a given r^*, independent of unit cell size. The cubic unit cell can access nearly the full range of porosity, with a lower limit of approximately 0.05 at $r^* = 0.5$, at which point the struts fully enclose the remaining void space. The Kelvin cell shows a similar void closure at a lower r^* of approximately 0.27, while the rate of change in porosity is greater in magnitude compared to the cubic unit cell. To show the specific surface area in a dimensionless form, it is scaled by cell length, and again, self-similarity exists across cell length scales. For a given r^*, specific surface area scales as a function of l_c. In addition, the local maximum in specific surface area corresponds to the porosity inflection point. For the Kelvin cell geometry specifically, the maximum corresponds to the r^* value at which the smallest window is closed by overlapping struts. More details regarding the window dimensions are available in Section 2 of Data S1. These trends are consistent with previous reports and expand the Kelvin lattice description to include the configurations in which the central window is closed.[29,35,36]

In the context of fluid dynamics, hydraulic diameter is another critical dimension.[30,37] Defined as $4\varepsilon/a_v$, it can also be scaled by the unit cell dimension to produce a self-similar profile, shown in Figure 3C. Given a target hydraulic diameter, any lattice geometry has two degrees of freedom (l_c, r^*) to achieve the desired dimension, resulting in a number of possible solutions where multiple lattice configurations satisfy the criterion. Furthermore, the satisfactory configurations may exhibit different degrees of porosity and other geometric properties. These results suggest that common trends exist for ordered structures of all types, supporting the potential for objective-based optimization of these cellular structures for a variety of multifunctional applications.

However, bulk geometric characteristics of lattices in functional parts may depart from single-cell characteristics, depending on the relative length scales. Because the process of forming a lattice geometry into a usable part requires trimming or adapting struts at the part boundary, the final properties of the part depend not only on the geometric features of a single cell but also where the struts are trimmed within the cell and how cell dimensions are adapted to the overall structure. This can have implications for fluid phenomena and analytical predictions of pressure drop if the single-cell values are inappropriately taken as representative of the entire part. Figure 4 (symbols with no border) shows the porosity and specific surface area of the latticed parts, as calculated by the CAD mesh files. For both lattices, porosity approaches the single-cell value with increasing system size, reaching the target value after the overall scale is greater than 20 l_c. Specific surface area exhibits a similar trend, but there is an offset deviation from the single-cell value even at the largest overall scale. Because of the truncated beams, using exclusively single-cell values does not result in an accurate description of the overall lattice properties at these length scales. For higher-density geometries like the Kelvin cell, lattice parts reached single-cell values before lower-density alternatives. However, both geometries exhibited approximately 2% deviation from single-cell porosity and 20% or less deviation from single-cell specific surface area by an overall scale of 10 l_c. These results may vary depending on the r^* configuration, but here specific surface area is more sensitive to truncation than porosity. As a result, fluids passing through the medium could see similar void spaces with relatively greater surface areas. This results in more significant changes to the hydraulic diameter as the overall system size scales down to smaller values of D/l_c, which contributes to apparent changes in pressure gradient. These results highlight the importance of considering the overall system scale when designing latticed parts for targeted parameters impacting fluid flows and scaling lattices up or down.

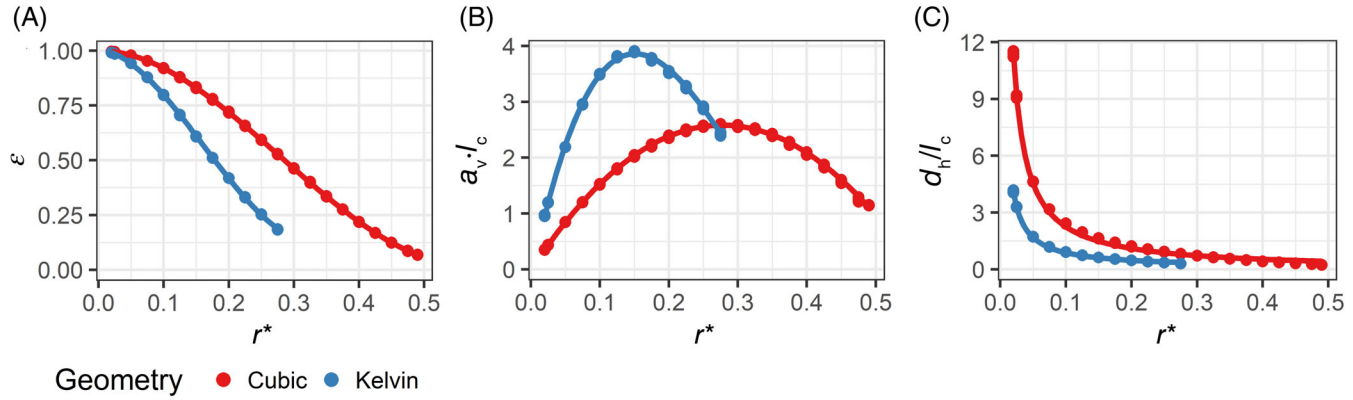

FIGURE 3 Theoretical values of (A) porosity, (B) specific surface area (dimensionless), and (C) hydraulic diameter (dimensionless) shown for cubic and Kelvin single unit cells with edge lengths ranging from 1 to 5 mm. Self-similarity across length scales is apparent when scaling by the unit cell edge length

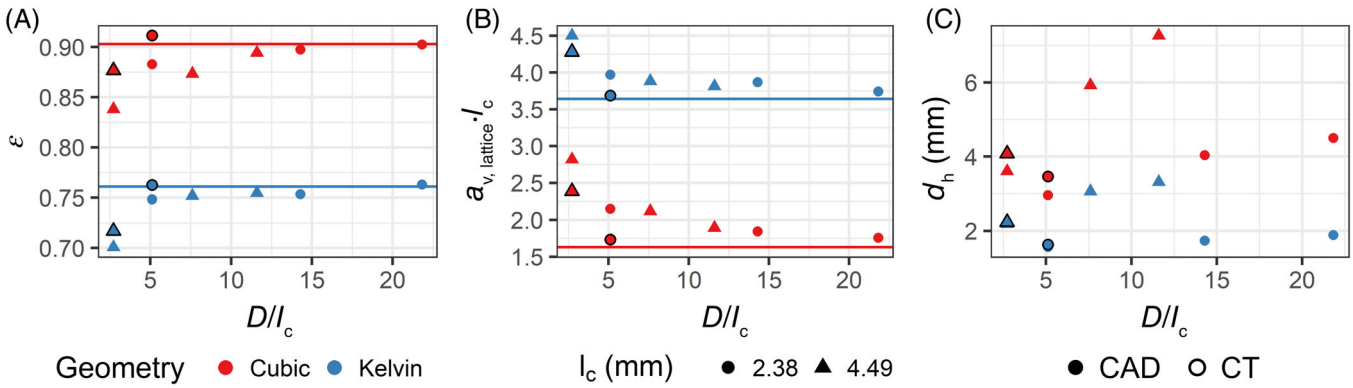

FIGURE 4 CAD-based (solid, no outline) and CT-based (black outline) geometric properties of lattice parts for the tested scales. (A) porosity (ε) and (B) dimensionless specific surface area ($a_{v,lattice}\ l_c$) shown for each cell length and lattice geometry, relative to the single-cell values for the respective configurations (horizontal lines). (C) Hydraulic diameter shown for each configuration, calculated using the total surface area. For subsequent calculations, CT-based measurements were applied to larger parts by scaling the CAD porosity and lattice surface area. CAD, computer-aided design; CT, computed tomography

Finally, we examined the difference in bulk properties between the as-designed CAD model and the as-printed, CT-scanned model. CT scanning has grown in popularity in additive manufacturing spaces because it permits noninvasive, nondestructive metrology for quality control and characterization. This is useful for analyzing part dimensions and determining internal heterogeneities that may create weak points or other defects in additively manufactured parts. Unlike other additive platforms, Carbon's continuous liquid interface production (CLIP™) technology creates parts that are fully solid and internally homogeneous, but vat photopolymerization techniques may still result in dimensional deviations.[38] Because these parts are entirely polymeric, the low-density material and high air content can result in reduced contrast, which may contribute to measurement deviations. However, the printer resolution and CT resolution are, respectively, 5× and 25× smaller than the smallest positive lattice features, which should lead to sufficient representation. Due to the computational demand of CT reconstruction and analysis, only the smallest lattice parts were selected for analysis. The dimensions of the scanned sections are shown in parentheses in Table 1 and Figure 4 (symbols with black outline), and images of the reconstructed parts are shown in Section 3 of Data S1. Printed lattices deviated in both porosity and specific surface area compared to the designed dimensions. These measured deviations may occur either from the additive manufacturing process or as an artifact of the CT reconstruction, which does not fully describe part roughness because of resolution differences between surface features and the imaging modality.[39] However, the increased porosity and decreased specific surface area are consistent with generalized beam thinning, a result of processing phenomena that lead to part shrinkage or overcuring, yielding deviations from designed dimensions.[38,40] Furthermore, it has been reported that dimensional variability can occur heterogeneously throughout the space of the part, but three dimensional compensation for these artifacts is beyond the scope of this work.[41] Here, we assumed that any spatial gradients were negligible in comparison to the length scales studied. For calculations requiring dimensions of larger latticed parts, we assumed similar deviations in the larger parts and applied a scaling

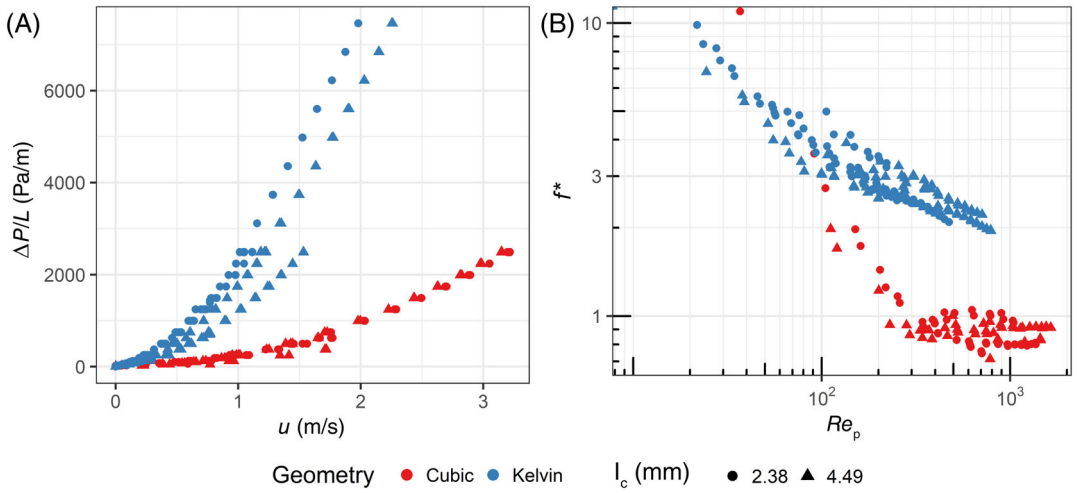

FIGURE 5 (A) Results of the pressure gradient measurements for lattice geometries in various configurations. Foam-like geometries produce higher pressure gradients, and differences between pipe scales are more pronounced for larger cell sizes. (B) Friction factor dependence on Re_p for both lattice types at all pipe scales. *Re*-independence indicates turbulent flow for cubic lattices, while Kelvin lattices do not reach a turbulent regime under the conditions tested

factor to their geometrical properties based on the ratio between design and CT measurements for the 12-mm lattices. For application of the POCS model to cubic lattices, we assumed that changes in the area porosity were negligible compared to the changes in other geometric properties. Overall, these results emphasize the importance of characterizing part geometry at various stages of production. Variation from targeted lattice attributes can result from both the manufacturing process and the characterization tools, highlighting persistent challenges in implementing such latticed parts based on exclusively a priori designs.

3.2 | Pressure behavior in scaled systems

Previous studies of cubic and Kelvin structures have examined pressure behavior largely in terms of porosity, varying the lattice configurations to achieve a typical porosity of 0.80–0.85.[29,42] Through comparisons to other models of porous media, these earlier studies show that porosity alone is not sufficient to describe the pressure behavior. Because additively manufactured periodic structures are commonly designed in terms of cell size and element thickness, we were interested in the resulting behavior when the design parameters such as cell size and strut dimension are held constant, and the only changing input is the unit cell configuration. This will not only support development and validation of the predictive models previously described but also facilitate an established process for comparing geometries not yet evaluated in the literature.

The results of the pressure experiments are shown as a function of superficial velocity in Figure 5A. Across all parts, the pressure gradient follows a parabolic trend consistent with the Ergun-like correlations presented. As expected from the porosity and surface area dependence, the increased surface area and decreased porosity in the Kelvin cell lattices yielded higher pressure gradients in all comparisons to cubic lattices. Smaller unit cell lengths showed increased pressure gradients across the column length. Furthermore, parts with the same geometry class and cell scale showed similar trends across length scales, with smaller l_c parts showing more similarity across pipe scales than larger l_c parts. These deviations between results from the small pipe and larger pipes for the larger unit cell length are consistent with the trends shown in Figure 4 caused by truncation of the lattice geometry. Based on second-order linear models fit to each system, the cubic unit cell lattices had a statistically significant viscous contribution to the pressure drop only when measured at lower flow rates and a statistically significant inertial contribution for all conditions. The Kelvin lattices had significant viscous and inertial contributions. These are consistent with their respective analytical model assumptions, as shown in Equations (1) and (2). Illustrating the differences in bulk properties between pipe scales, fitted models for each of the configurations showed statistically significant differences between pipe sizes at $p < 0.05$ (Section 8 of Data S1). For other types of additively manufactured porous media, the hydraulic diameter has been identified as a critical parameter for system scaling.[37] In line with these previous findings, the differences in pressure behavior observed between overall system scales are most prominent when there is a significant change in hydraulic diameter. These results suggest that an overall system diameter of 10 l_c or greater is best suited to reduce the effects of deviations in hydraulic diameter and achieve representative outcomes of a larger system when using a small-scale system.

In considering the operating flow regime, we calculated the modified friction factor for a packed bed over the experimental range, as shown in Figure 5B as a function of the modified *Re* for a packed bed (Re_p). Where not yet turbulent, the friction factor exhibited a dependence on *Re* until turbulent flow was established. Based on the near-constant friction factor for the cubic lattice structures at $Re_p > 300$, these are likely in an established turbulent regime. However, for the Kelvin lattices under comparable system conditions, the friction factor

exhibits *Re*-dependence, indicating that flow is not yet turbulent. Compared to previous reports for similar structures, the Kelvin geometry exhibits *Re*-independent friction factor at a similar order of magnitude for $Re_p > 500$, which is higher than the conditions examined here.[42] These differences may arise from the different manufacturing processes used to create the idealized foams in the prior work, since metal 3D printing is known to introduce additional roughness on the part surfaces.[39] In light of this, it is likely that the Kelvin lattices under these conditions in our study are in the post-Forchheimer regime.[43] Combined with the cubic results, the data suggest that in systems where the packing structure is an available degree of freedom, selection between different lattice geometries with identical design parameters yields not only different geometric features but also different flow characteristics. However, it is important to note that even when parameters like porosity, specific surface area, and hydraulic diameter are comparable between structures, factors such as tortuosity can have a significant influence on the pressure gradient.[29,44] Indeed, the smaller tortuosity expected from cubic lattices compared to Kelvin lattices likely amounts to the increased friction factors observed in Kelvin lattices where the two geometries have otherwise comparable features and operating conditions.

To confirm whether the results presented here were consistent with the semi-empirical correlations developed for ordered lattices, we compared the cubic lattices to the model proposed for POCS and the Kelvin lattices to the model proposed for tortuous open-cell foams. Both models work largely from the same geometric characteristics. One notable difference reported by the authors of the foam model is its inclusion of the system walls in the specific surface area term. Furthermore, the POCS model has been demonstrated only for cubic lattices, and it neglects viscous contributions to the pressure gradient. Since the lattice size ranges in this work are similar to the systems used to validate the models, we expected reasonable agreement between the correlation predictions and experimental values (within 30% error, in line with original reporting). Based on the geometric characterization, we expected to see slight differences between predictions for each unit cell configuration at the various pipe scales, due to beam truncation. We further hypothesized that using the properties derived from CT reconstruction would improve agreement between the experimental values and correlation predictions.

First, we compared the experimental data to the as-reported analytical model predictions from Equations (1)–(3). The input parameters for each prediction were based on the CT-derived geometric properties for the 12-mm-diameter lattices, scaled to the respective system size. The results are represented as a parity plot shown in Figure 6A. Model estimates underpredicted cubic lattice results and overpredicted Kelvin lattice results. The POCS model tended to underestimate the experimental values by 30% or more, indicated by the lighter shaded region. The foam model overpredicted the pressure gradient in Kelvin lattices by 30% or more for both cell scales, with the exception of the 52-mm system. Imaging-related factors, including contrast differences from CT imaging on high-porosity parts, thresholding, and reconstruction methods, can contribute to differences between true

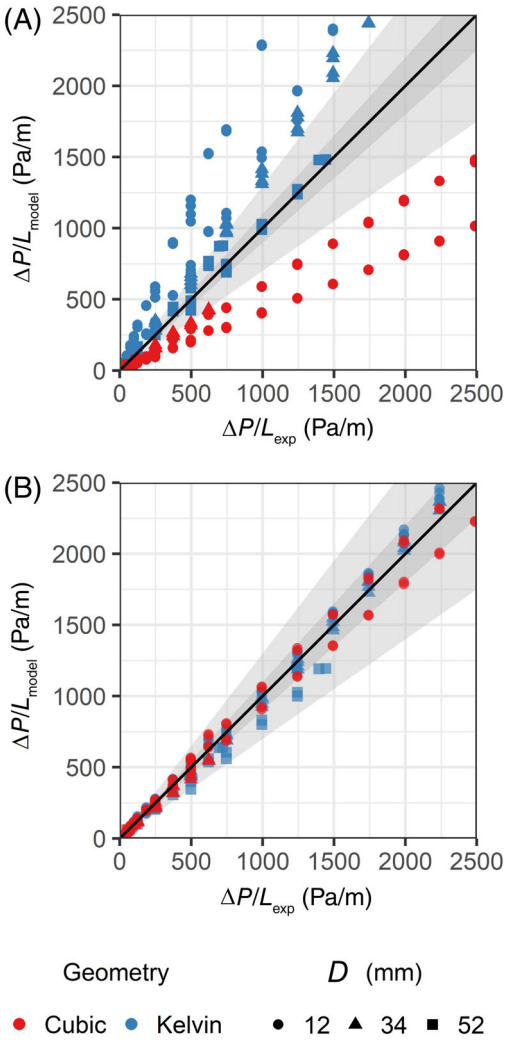

FIGURE 6 (A) Parity plot comparing CT-based model prediction with experimental values, using the literature models for the respective lattice type (Kelvin-foam; cubic-POCS). (B) Foam model adjusted for cubic and Kelvin geometric properties. Cubic tortuosity was approximated by CAD-derived geometric tortuosity ($\tau = 1.01$), and Kelvin tortuosity was taken as $\tau = 1.41$ for all relevant lattices, based on the observed porosity and the correlation proposed by Inayat et al.[30] Shaded regions indicate ±10% and ±30% deviations from the experimental values. CAD, computer-aided design; CT, computed tomography; POCS, periodic open cellular structure

geometric properties and the values calculated by CT, as described in the previous section. The differences here may be attributed to the smooth surfaces produced by the CLIP™ process, as compared to other additive processes.[45–47] Furthermore, since these parts are polymeric, not ceramic or metallic, the reduced contrast may limit feature detection, even at high resolution. Therefore, these results do not necessarily imply model disagreement, but they highlight a challenge in developing predictive models and correlations based on these measurements alone.

Because of the differences in CT-based predictions and uncertainty regarding wall influences, we further considered the analytical

models in terms of the other available quantities. Results for the as-designed geometric porosity and the surface area are shown with and without wall surface contributions in Section 5 of Data S1. However, the most promising prediction came from adapting the hydraulic diameter, porosity, and tortuosity of the foam model to each lattice. Figure 6B shows model parity results when using the foam model described in Equation (2) with the tortuosity parameter adjusted for each unit cell geometry. To estimate the tortuosity of each structure, we first generated a CAD simulation of a series of paths passing over the struts of a single unit cell for both cubic and Kelvin geometries as described in Section 2. Based on these calculations for $r^* = 0.11$, the cubic tortuosity was estimated to be approximately 1.01, and the Kelvin tortuosity was estimated to be approximately 1.05, which is comparable to a previous estimate for a Kelvin lattice under similar conditions.[44] A combination of path length tortuosity and geometric tortuosity was selected because it can be calculated from static geometric characteristics and does not depend on flow conditions.[48] However, as a result, it is an underestimate of the actual hydrodynamic tortuosity that influences the pressure gradient.[48] For cubic lattices, agreement between the cubic model prediction and experimental data in the parity plot in Figure 6B implies that the hydrodynamic tortuosity for this geometry is in fact near unity. However, for Kelvin lattices, the pressure gradient predictions using the estimated tortuosity underestimate the behavior by greater than 30% (shown in Section 5 of Data S1). Given the results calculated for each specific surface area case (used in Figure 6A), the actual hydrodynamic tortuosity value is expected to be higher than calculated using the static geometric characteristics. This is inline with updated calculations of tortuosity in open foams from Inayat et al., who report an effective hydrodynamic tortuosity of approximately 1.41 for a Kelvin lattice with $\varepsilon = 0.76$ and cylindrical struts.[30] Applying this tortuosity value for the Kelvin lattice is reflected in the parity plot in Figure 6B, which resulted in substantial improved agreement of the model prediction with experimental data. Thus overall, model predictions are improved to a deviation of 30% or less when using the foam model with a single-cell tortuosity estimate for all lattices of the same unit cell type. For the cubic unit cell, there is a departure from model fit at lower *Re*, which suggests that more complex phenomena are occurring. Furthermore, in the event that the central Kelvin pores close during design or processing, the tortuosity would continue to increase, but the hydraulic tortuosity may no longer follow the prescribed trend. Thus, the opportunity for a fully unifying model remains, but based on these results, it is sufficient to estimate the pressure gradient across a range of length scales using the geometric properties estimated from CAD models informed by CT scans.

3.3 | Pressure behavior in combination systems

Since these structures can be designed for an arbitrary configuration, it is theoretically possible to tailor the overall structure to any given application when intermediate properties are desirable. Where a range of properties is desired in a localized region, functional grading is a common additive manufacturing technique used to transition between one configuration and another.[49,50] Combining different lattice geometries directly is another strategy for producing intermediate bulk properties between lattice archetypes or producing distinct regional conditions within a single system. Through direct combination of different lattices, rather than gradual functional grading, we propose the possibility of modular components for scaling processes up and out. Combining distinct lattice geometries in series would be expected to yield linearly additive pressure gradients for tunable control. To evaluate this hypothesis and examine the behavior for these systems, each combination of the four original lattice types was assembled and tested in the 12-mm system. This pipe scale was selected to facilitate alignment of the lattice parts and material efficiency in early testing phases, which can be useful for lab-scale processes.

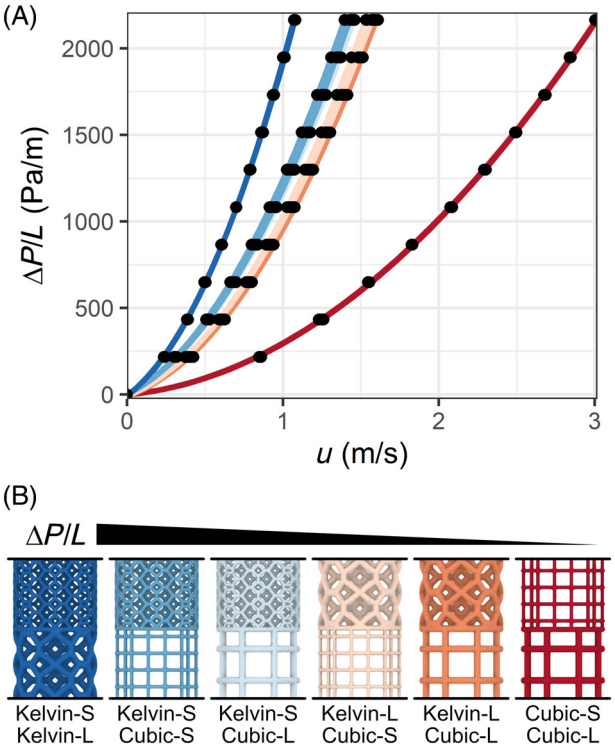

FIGURE 7 (A) Pressure gradient results for the elongated stack combinations in the as-depicted and inverted orientations. (B) Order of lattice combinations by observed pressure gradient

Experimental results evaluating pressure drop across the combination stacks, combined with a limited set of CFD studies on single unit cells and lattice stacks, suggested that entrance effects and orientation play a significant role in driving complex pressure gradients (Sections 6 and 7 of Data S1). A single Cubic-S|Cubic-L combination lattice aligned digitally and printed continuously was capable of a lower pressure gradient compared to the equivalent manually aligned stack (Section 6 of Data S1), suggesting that even slight offsets introduced by manual alignment can result in noticeable deviations from the ideal pressure gradient. Such increased pressure gradients resulting from alignment differences has also been observed in rotated lattices and interpenetrating lattice systems.[29,51] To experimentally evaluate the

intralattice phenomena away from possible entrance or exit regions, two 100-mm lattice columns were manually aligned and oriented at the center of the measurement zone. This permitted measurement of the pressure gradient directly within the lattice structure, which is a unique feature of this approach to lattice generation and not possible when using a solid wall around the part. The results of these experiments are shown in Figure 7A for the as-depicted and inverted orientations. Because these parts were not perfectly aligned for the print step, the observed pressure gradient may have deviated from the ideal value. However, the trends followed as expected from the single-lattice parts. As with single-lattice parts, the Kelvin cell combination exhibited the highest pressure gradient, and the cubic combination exhibited the lowest pressure gradient, with other combinations populating the space between. Incremental changes in lattice combinations showed changes in pressure gradient that followed the uniform columns, where smaller length scales increase the pressure gradient, and the Kelvin geometry increases the pressure gradient. This phenomenon is easily visualized by the smooth transition in the diverging color scale in Figure 7A. Figure 7B illustrates the pressure gradient trends graphically with representations of the lattice parts.

The cubic-only lattice combinations (Cubic-S|Cubic-L, Cubic-L|Cubic-S*) do not show orientation dependence, suggesting that they are well aligned, even with two distinct parts. This was evaluated by ANOVA, as described in the experimental methods. All other combinations of manually aligned lattices showed some degree of orientation dependence of the sequential stacks as determined by the minimized error in the model including the orientation parameters. Further examining the coefficients of these models, Kelvin-S|Cubic-L and Kelvin-L|Cubic-L did not have any individual interaction terms significant at $p < 0.05$, but the ANOVA results indicated better model fit from the combined influences of orientation. All remaining combinations (Kelvin-L|Cubic-S, Kelvin-S|Cubic-S, and Kelvin-S|Kelvin-L) had significant interactions between orientation and inertial terms but not viscous terms in the polynomial. These results combined suggest that the orientation dependence is more pronounced at higher velocities and may still be related to flow development phenomena.

The finding that only the cubic-only system is fully orientation-independent under these conditions is consistent with the observations of the friction factor (Figure 5B), where the cubic results suggested a turbulent regime under the same conditions where Kelvin cells were in a laminar or transition regime. Because of this, the interaction between the two geometries would be subject to flow development in at least one part of the combination. Previous investigations into lattice combinations at the single unit cell level suggest that pressure drop can be predicted a priori based on theoretical or empirically determined values for a single geometry.[27,51] In this work, we observed experimentally and inferred from the statistical models that the pressure gradient contributions from each half of the lattice column are not linearly additive. The model coefficients for all inertial terms were statistically significantly different from the theoretical model parameters based on the single-lattice packings. The viscous term coefficients for all cubic-Kelvin combinations did not show statistically significant differences, but Kelvin-S|Kelvin-L and Cubic-S|Cubic-L lattices showed statistically significant differences in this regard. Statistical significance was determined by comparing the 95% confidence intervals of the coefficients at the theoretical average for both orientations. This suggests that there may be more complex flow profiles that develop between lattices in series, influenced by tortuosity, but more investigation is needed to confirm the entrance and orientation effects. Based on these observations, separated lattice segments offer another alternative for *in operando* flow adjustment based on changes to system tortuosity, creating an opportunity to design dynamic systems with unique characteristics that would not be achievable with a single lattice alone.

4 | CONCLUSION

3D printing and its associated technologies provide an unprecedented level of geometric complexity in manufactured parts. It facilitates control over transport phenomena in ways that can be modeled and predicted for complex channel networks or highly ordered packings, which promise high-throughput production and rationally designed systems for nearly any application. In order to realize that capability, advanced models need to account for the internal structure, the overall system scale, and interactions between these highly ordered domains.

To that end, we have described the scaling behavior of cellular lattice structures in terms of geometric properties and pressure gradients. Across length scales, we demonstrate self-similarities for pore dimensions, porosity, specific surface area, and hydraulic diameter, where the latter two parameters scale linearly with cell length for a given dimensionless strut radius. We show that lattice structures have unique geometric properties, which can facilitate optimization and lattice selection for a given application. In terms of overall system size, we show that a system diameter 10 times greater than the cell length is sufficient to estimate overall geometric properties based on those of a single unit cell, but the differences in hydraulic diameter must still be accounted for in system modeling. While further development is needed to achieve a unifying correlation, we confirm experimentally that a single pressure drop correlation can fit both the cubic and Kelvin lattice geometries within approximately 30% deviation from most experimental values, given appropriate substitution of lattice-specific geometric quantities. Furthermore, we find that sufficient prediction is yielded by using the geometric properties of the lattice structure based on the CAD design when informed with print deviations, which can limit the necessity of resource-intensive micro-CT metrology.

Experiments in combination systems suggest that pressure gradients within the combined column are largely orientation dependent but may depend on length scale. The pressure gradient and flow profiles can be sensitive to entrance regions within the lattice structures, which may exceed the length of a single unit cell, contributing to orientation dependence in shorter columns. Furthermore, the overall pressure gradient in a combination system is not necessarily the weighted sum of the individual contributions. Further work is necessary to understand the effects of combining different lattice structures in more complex arrangements, how these phenomena interact at larger overall system scales, and how

peripheral lattice design influences wall phenomena. Nonetheless, this work represents a critical step in understanding the behavior of advanced packing structures and builds towards their potential as a platform for highly flexible and scalable process systems.

NOTATION

a_v	specific surface area, lattice surface area/total geometric volume
D	overall system diameter
d_h	hydraulic diameter (4·wetted perimeter/cross sectional flow area)
$d_{p,eq}$	equivalent particle diameter, based on the ratio of lattice surface area to lattice solid volume
d_w	window diameter
L	length of the lattice column in the measurement region
l_c	unit cell edge length
Q	volumetric flow rate
r	strut radius
r^*	dimensionless strut radius, r/l_c
u	superficial velocity
ε	porosity (void fraction), void volume/total volume
ε_A	area porosity (void fraction), projected void area/projected solid area
μ	fluid viscosity (kg/[m·s])
ρ	fluid density (kg/m^3)
τ	tortuosity (effective path length/minimum path length)
CAD	computer-aided design
CT	computed tomography
Re	Reynolds number ($d{\cdot}v{\cdot}\rho/\mu$)
CLKS	combination naming (top–bottom; cubic large–Kelvin small)

ACKNOWLEDGMENTS

The authors would like to thank Emily Rose Williams of Carbon, Inc. for helpful insights regarding resin selection. This study was supported by the National Institutes of Health and the State of Delaware under Award Numbers P20GM104316 and U54-GM104941. The content is solely the responsibility of the authors and does not necessarily represent the official views of the National Institutes of Health.

DATA AVAILABILITY STATEMENT

The data that support the findings of this study are available from the corresponding author upon reasonable request.

ORCID

Ian R. Woodward https://orcid.org/0000-0003-4471-3734
Lucas Attia https://orcid.org/0000-0002-9941-3846
Catherine A. Fromen https://orcid.org/0000-0002-7528-0997

REFERENCES

1. Li N, Huang S, Zhang G, et al. Progress in additive manufacturing on new materials: a review. *Journal of Materials Science & Technology*. 2019;35(2):242-269.
2. Parra-Cabrera C, Achille C, Kuhn S, Ameloot R. 3D printing in chemical engineering and catalytic technology: structured catalysts, mixers and reactors. *Chem Soc Rev*. 2018;47(1):209-230.
3. Kalsoom U, Nesterenko PN, Paull B. Current and future impact of 3D printing on the separation sciences. *TrAC Trends Anal Chem*. 2018;105:492-502.
4. Roper CS, Schubert RC, Maloney KJ, et al. Scalable 3D bicontinuous fluid networks: polymer heat exchangers toward artificial organs. *Adv Mater*. 2015;27(15):2479-2484.
5. Lawson S, Li X, Thakkar H, Rownaghi AA, Rezaei F. Recent advances in 3D printing of structured materials for adsorption and catalysis applications. *Chem Rev*. 2021;121(10):6246-6291.
6. Oh HJ, Aboian MS, Yi MYJ, et al. 3D printed absorber for capturing chemotherapy drugs before they spread through the body. *ACS Cent Sci*. 2019;5(3):419-427.
7. Germain L, Fuentes CA, van Vuure AW, des Rieux A, Dupont-Gillain C. 3D-printed biodegradable gyroid scaffolds for tissue engineering applications. *Mater Design*. 2018;151:113-122.
8. Dong G, Tang Y, Li D, Zhao YF. Design and optimization of solid lattice hybrid structures fabricated by additive manufacturing. *Addit Manuf*. 2020;33:101116.
9. Frenzel T, Kadic M, Wegener M. Three-dimensional mechanical metamaterials with a twist. *Science*. 2017;358(6366):1072-1074.
10. Coulais C, Teomy E, de Reus K, Shokef Y, van Hecke M. Combinatorial design of textured mechanical metamaterials. *Nature*. 2016;535(7613):529-532.
11. Kolewe EL, Feng Y, Fromen CA. Realizing lobe-specific aerosol targeting in a 3D-printed in vitro lung model. *J Aerosol Med Pulm Drug Deliv*. 2021;34(1):42-56.
12. Park YJ, Yu T, Yim SJ, You D, Kim DP. A 3D-printed flow distributor with uniform flow rate control for multi-stacked microfluidic systems. *Lab Chip*. 2018;18(8):1250-1258.
13. Zhang H, Kopfmüller T, Achermann R, et al. Accessing multi-dimensional mixing via 3D printing and showerhead micromixer design. *AIChE J*. 2019;66(4):e16873.
14. Biedermann M, Meboldt M. Computational design synthesis of additive manufactured multi-flow nozzles. *Addit Manuf*. 2020;35:101231.
15. Ashby MF. The properties of foams and lattices. *Philos Trans A Math Phys Eng Sci*. 2006;364(1838):15-30.
16. Hanks B, Berthel J, Frecker M, Simpson TW. Mechanical properties of additively manufactured metal lattice structures: data review and design interface. *Addit Manuf*. 2020;35:101301.
17. Jiang Y, Wang Q. Highly-stretchable 3D-architected mechanical metamaterials. *Sci Rep*. 2016;6:34147.
18. Pelanconi M, Barbato M, Zavattoni S, Vignoles GL, Ortona A. Thermal design, optimization and additive manufacturing of ceramic regular structures to maximize the radiative heat transfer. *Mater Design*. 2019;163:107539.
19. Sinn C, Wentrup J, Pesch GR, Thöming J, Kiewidt L. Structure-heat transport analysis of periodic open-cell foams to be used as catalyst carriers. *Chem Eng ResDesign*. 2021;166:209-219.
20. Rezaei E, Barbato M, Gianella S, Ortona A, Haussener S. Pressure drop and convective heat transfer in different SiSiC structures fabricated by indirect additive manufacturing. *J Heat Transfer*. 2020;142(3):032702.
21. Zhianmanesh M, Varmazyar M, Montazerian H. Fluid permeability of graded porosity scaffolds architectured with minimal surfaces. *ACS Biomater Sci Eng*. 2019;5(3):1228-1237.
22. Bathla P, Kennedy J. 3D printed structured porous treatments for flow control around a circular cylinder. *Fluids*. 2020;5(3):136.
23. Fee C, Nawada S, Dimartino S. 3D printed porous media columns with fine control of column packing morphology. *J Chromatogr A*. 2014;1333:18-24.
24. Dolamore F, Fee C, Dimartino S. Modelling ordered packed beds of spheres: the importance of bed orientation and the influence of tortuosity on dispersion. *J Chromatogr A*. 2018;1532:150-160.

25. Busse C, Freund H, Schwieger W. Intensification of heat transfer in catalytic reactors by additively manufactured periodic open cellular structures (POCS). *Chem Eng Process Process Intens*. 2018;124:199-214.
26. Lucci F, Della Torre A, Montenegro G, Eggenschwiler PD. On the catalytic performance of open cell structures versus honeycombs. *Chem Eng J*. 2015;264:514-521.
27. Lämmermann M, Horak G, Schwieger W, Freund H. Periodic open cellular structures (POCS) for intensification of multiphase reactors: liquid holdup and two-phase pressure drop. *Chem Eng Process Process Intens*. 2018;126:178-189.
28. Pellejero I, Almazán F, Lafuente M, et al. Functionalization of 3D printed ABS filters with MOF for toxic gas removal. *J Indus Eng Chem*. 2020;89:194-203.
29. Klumpp M, Inayat A, Schwerdtfeger J, et al. Periodic open cellular structures with ideal cubic cell geometry: effect of porosity and cell orientation on pressure drop behavior. *Chem Eng J*. 2014;242:364-378.
30. Inayat A, Klumpp M, Lämmermann M, Freund H, Schwieger W. Development of a new pressure drop correlation for open-cell foams based completely on theoretical grounds: taking into account strut shape and geometric tortuosity. *Chem Eng J*. 2016;287:704-719.
31. Lucci F, Della Torre A, Montenegro G, Kaufmann R, Eggenschwiler PD. Comparison of geometrical, momentum and mass transfer characteristics of real foams to Kelvin cell lattices for catalyst applications. *Int J Heat Mass Transfer*. 2017;108:341-350.
32. Dudukovic NA, Fong EJ, Gemeda HB, et al. Cellular fluidics. *Nature*. 2021;595(7865):58-65.
33. Fedorov A, Beichel R, Kalpathy-Cramer J, et al. 3D slicer as an image computing platform for the quantitative imaging network. *Magn Reson Imaging*. 2012;30(9):1323-1341.
34. Bracconi M, Ambrosetti M, Okafor O, et al. Investigation of pressure drop in 3D replicated open-cell foams: coupling CFD with experimental data on additively manufactured foams. *Chem Eng J*. 2019;377:120123.
35. Lucci F, Della Torre A, von Rickenbach J, Montenegro G, Poulikakos D, Eggenschwiler PD. Performance of randomized Kelvin cell structures as catalytic substrates: mass-transfer based analysis. *Chem Eng Sci*. 2014;112:143-151.
36. Tanlak N, De Lange DF, Van Paepegem W. Numerical prediction of the printable density range of lattice structures for additive manufacturing. *Mater Design*. 2017;133:549-558.
37. Dolamore F, Dimartino S, Fee CJ. Numerical elucidation of flow and dispersion in ordered packed beds: nonspherical polygons and the effect of particle overlap on chromatographic performance. *Anal Chem*. 2019;91(23):15009-15016.
38. Westbeek S, Remmers JJC, van Dommelen JAW, Maalderink HH, Geers MGD. Prediction of the deformed geometry of vat photopolymerized components using a multi-physical modeling framework. *Addit Manuf*. 2021;40:101922.
39. Van Bael S, Kerckhofs G, Moesen M, Pyka G, Schrooten J, Kruth JP. Micro-CT-based improvement of geometrical and mechanical controllability of selective laser melted Ti6Al4V porous structures. *Mater Sci Eng A*. 2011;528(24):7423-7431.
40. Dean D, Jonathan W, Siblani A, et al. Continuous digital light processing (cDLP): highly accurate additive manufacturing of tissue engineered bone scaffolds. *Virtual Phys Prototyp*. 2012;7(1):13-24.
41. McGregor DJ, Tawfick S, King WP. Automated metrology and geometric analysis of additively manufactured lattice structures. *Addit Manuf*. 2019;28:535-545.
42. Inayat A, Schwerdtfeger J, Freund H, Körner C, Singer RF, Schwieger W. Periodic open-cell foams: pressure drop measurements and modeling of an ideal tetrakaidecahedra packing. *Chem Eng Sci*. 2011;66(12):2758-2763.
43. Della Torre A, Montenegro G, Tabor GR, Wears ML. CFD characterization of flow regimes inside open cell foam substrates. *Int J Heat Fluid Flow*. 2014;50:72-82.
44. Habisreuther P, Djordjevic N, Zarzalis N. Statistical distribution of residence time and tortuosity of flow through open-cell foams. *Chem Eng Sci*. 2009;64(23):4943-4954.
45. Janusziewicz R, Tumbleston JR, Quintanilla AL, Mecham SJ, DeSimone JM. Layerless fabrication with continuous liquid interface production. *Proc Natl Acad Sci USA*. 2016;113(42):11703-11708.
46. Lozanovski B, Downing D, Tino R, et al. Image-based geometrical characterization of nodes in additively manufactured lattice structures. *3D Print Addit Manuf*. 2021;8(1):51-68.
47. Echeta I, Feng X, Dutton B, Leach R, Piano S. Review of defects in lattice structures manufactured by powder bed fusion. *Int J Adv Manuf Technol*. 2019;106(5–6):2649-2668.
48. Clennell MB. Tortuosity: a guide through the maze. *Geol Soc Lond Spec Publ*. 1997;122(1):299-344.
49. Loh GH, Pei E, Harrison D, Monzón MD. An overview of functionally graded additive manufacturing. *Addit Manuf*. 2018;23:34-44.
50. Cipriani CE, Ha T, Martinez Defilló OB, et al. Structure–processing–property relationships of 3D printed porous polymeric materials. *ACS Mater*. 2021;1:69-80.
51. Do G, Geißelbrecht M, Schwieger W, Freund H. Additive manufacturing of interpenetrating periodic open cellular structures (interPOCS) with in operando adjustable flow characteristics. *Chem Eng Process Process Intens*. 2020;148:107786.

SUPPORTING INFORMATION

Additional supporting information may be found in the online version of the article at the publisher's website.

How to cite this article: Woodward IR, Attia L, Patel P, Fromen CA. Scalable 3D-printed lattices for pressure control in fluid applications. *AIChE J*. 2021;e17452. doi: 10.1002/aic.17452